

Exceptional entanglement transition and natural-dissipation-enhanced quantum sensing

Peirong Han^{1,*}, Fan Wu^{1,*}, Xinjie Huang^{1,*}, Huaizhi Wu¹, Chang-Ling Zou^{2,3,8},
Wei Yi^{2,3,8}, Mengzhen Zhang⁴, Hekang Li⁵, Kai Xu^{5,6,8}, Dongning Zheng^{5,6,8},
Heng Fan^{5,6,8}, Jianming Wen^{7,†}, Zhenbiao Yang^{1,8,‡} and Shibiao Zheng^{1,8,§}

¹*Department of Physics, Fuzhou University, Fuzhou, Fujian,
350108, China*

²*CAS Key Laboratory of Quantum Information,
University of Science and
Technology of China, Hefei 230026, China*

³*CAS Center for Excellence in Quantum Information and Quantum Physics,
University of Science and Technology of China,
Hefei 230026, China*

⁴*Pritzker School of Molecular Engineering,
University of Chicago,
Chicago, IL 60637, USA*

⁵*Institute of Physics,
Chinese Academy of Sciences, Beijing 100190,
China*

⁶*CAS Center for Excellence in Topological Quantum Computation,
University of Chinese Academy of Sciences,
Beijing 100190, China*

⁷*Department of Physics,
Kennesaw State University, Marietta, Georgia
30060, USA*

⁸*Hefei National Laboratory, Hefei 230088, China*

Extension of Hamiltonian dynamics from the Hermitian to non-Hermitian (NH) domain has significantly advanced physical sciences. While classical aspects of NH physics have been substantially explored, investigations of exceptional phenomena uniquely associated with NH quantum-mechanically correlated systems are still lacking. Here we unveil an entanglement transition in naturally-dissipative light-matter systems at the exceptional point (EP), and experimentally demonstrate this phenomenon with a circuit quantum electrodynamics architecture. The results confirm the EP's quantum nature, and reveal its connection to exceptional entanglement behaviors, which are universal for NH interacting quantum systems, but have remained unexplored. We further demonstrate that the U(1) symmetry of our system enables the unavoidable natural dissipation, detrimental to conventional quantum sensing protocols, to serve as a positive resource for amplifying weak field effects.

When a physical system undergoes dissipation, the Hermiticity of its Hamiltonian dynamics is broken down. As any system inevitably interacts with its surrounding environment by exchanging particles or energy, non-Hermitian (NH) effects are ubiquitous in both classical and quantum physics. Such effects were once thought to be detrimental, and needed to be suppressed for observing physical phenomena of interest and for technological applications, until the finding that NH dynamics could represent a complex extension of quantum mechanics [1-3]. Since then, increasing efforts have been devoted to the exploration of NH physics, leading to discoveries of a number of intriguing phenomena that are inherent in NH systems, such as the parity-time (\mathcal{PT}) phase transition and exceptional topology, both associated to the exceptional points (EPs) where the eigenenergies as well as the eigenvectors of the NH Hamiltonian coalesce [4-6]. In addition to fundamental interest, such NH effects promise realization of enhanced sensors [7-11].

So far, there have been a plethora of experimental investigations on NH dynamics [12-20], as well as on relevant applications [21-25], which, however, are primarily focused on classically interacting but non-entangled systems. To gain a more fundamental understanding of NH physics and to exploit the associated emergent phenomena in quantum technology, exploring NH dynamics within a fully quantum-mechanical framework is essential. However, no such

*These authors contribute equally to this work.

†E-mail: jianming.wen@gmail.com

‡E-mail: zbyangmk@gmail.com

§E-mail: fjqiqo@fzu.edu.cn

experimental demonstrations have been reported to date, despite persistent efforts that have led to encouraging advances with different scenarios, ranging from optical systems [26-28] to ultracold atoms [29-31] and trapped ions [32,33], and from nitrogen-vacancy centers [34-36] to superconducting circuits [37-39]. These experiments have been confined to realizations of NH semiclassical models, where either the light or the matter degrees of freedom are treated classically in the dissipative, light-matter coupled system. Consequently, the EPs underlying the observed NH phenomena are of classical nature, without association to any quantum correlation.

In this study, we investigate in both theory and experiment exceptional phenomena in strongly correlated quantum systems, uncovering a hitherto unreported entanglement phase transition, occurring at the onset of the real-imaginary shift of the quantum Rabi splitting. Such a transition highlights the quantum character of the EP, and reveals a deep connection between nonclassical correlations and singular behaviors in composite quantum system governed by NH Hamiltonians. We experimentally demonstrate this exceptional transition in a circuit, where a superconducting qubit is controllably coupled to a decaying resonator. The exceptional entanglement signature is mapped out by a density matrix post-casting method, which enables us to extract the weak nonclassical signal from a strong noisy background. Additionally, the demonstrated NH phenomena originate from naturally occurring dissipation, rather than being induced by an artificially engineered dissipative channel [12-39]. This natural character not only makes the results universal for open quantum systems immersed in pervasive Markovian reservoirs, but also offers the possibility to turn the resulting dissipation from an unavoidable nuisance into a stable resource for enhancing quantum sensing. We demonstrate such a sensing scenario, where the physical quantity to be estimated is encoded in the qubit-resonator entangled state evolved by the natural-reservoir-associated NH Hamiltonian dynamics.

The model under consideration is composed of a decaying quantized field mode resonantly coupled to a two-level system (qubit) with a negligible decaying rate (Fig. 1a). The quantum state evolution trajectory without photon number jumps is governed by the NH Hamiltonian (setting $\hbar = 1$)

$$\mathcal{H}_{\text{NH}} = \Omega(a^\dagger |g\rangle \langle e| + a |e\rangle \langle g|) - \frac{i}{2}\kappa a^\dagger a, \quad (1)$$

where $|e\rangle$ ($|g\rangle$) denotes the upper (lower) level of the qubit, a^\dagger (a) represents the creation (annihilation) operator for the bosonic mode with a dissipation rate κ , and Ω is their coupling strength. The coupled qubit-field system bears a U(1) symmetry—the Hamiltonian remains invariant under the transformation $e^{i\phi(a^\dagger a + |e\rangle \langle e|)}$. This property enables the system dynamics to be restricted within the reduced Hilbert subspace $\{|e, n-1\rangle, |g, n\rangle\}$ ($n \geq 1$) when the system initially possesses n excitations. Here the number in each ket denotes the photon number of the resonator. In such a subspace, the system has two entangled eigenstates, given by

$$|\Phi_\pm\rangle = \mathcal{N}_\pm(\sqrt{n}\Omega |e, n-1\rangle + \Gamma_\pm |g, n\rangle), \quad (2)$$

which are separated by an energy gap of $E_G = 2\sqrt{n\Omega^2 - \kappa^2/16}$, with $\Gamma_\pm = -i\kappa/4 \pm E_G/2$. This quantum entanglement makes the system fundamentally distinct from previously demonstrated NH semiclassical models [29-39], where the qubit is not entangled with the classical control field in any way. When $\Omega > \kappa/(4\sqrt{n})$, the eigenspectrum has a real gap, and the system undergoes Rabi-like oscillations, during which the qubit periodically exchanges photons with the light field. With the decrease of Ω , the energy gap is continuously narrowed until reaching the EP, where the two energy levels coalesce. After crossing the EP, the gap becomes imaginary, and the population evolution exhibits an over-damping feature.

Unlike previous investigations, here each eigenenergy is possessed by the two entangled components, neither of which has its own state alone. The nonclassical feature of the composite system is manifested by the quantum entanglement of the underlying eigenstate, which can be quantified by the concurrence [40]

$$\mathcal{E}_\pm = \frac{2\sqrt{n}\Omega |\Gamma_\pm|}{|\Gamma_\pm|^2 + n\Omega^2}. \quad (3)$$

When $\kappa = 0$, the concurrences are independent of Ω as $\mathcal{E}_\pm \equiv 1$. The NH dynamics endows these eigenstates with unique characters that are otherwise inaccessible. When the rescaled coupling strength $\eta = 4\sqrt{n}\Omega/\kappa$ is much smaller than 1, the two eigenstates are respectively dominated by $|e, n-1\rangle$ and $|g, n\rangle$. With the increase of η , these two populations become increasingly balanced toward the EP at $\eta = 1$, where both eigenstates converge to the same maximally entangled state. During this convergence, \mathcal{E}_\pm exhibit a linear scaling with η . In the Bloch representation, this corresponds to a rotation of the eigenvector $|\Phi_+\rangle$ ($|\Phi_-\rangle$) around the x ($-x$) axis from pointing at the north (south) polar, until merging at the y axis, as shown in Fig. 1b. After crossing the EP, \mathcal{E}_\pm become independent of Ω , which implies both two eigenstates keep maximally entangled. However, $|\Phi_+\rangle$ ($|\Phi_-\rangle$) is rotated around the z ($-z$) axis, progressively approaching the x ($-x$) axis (Fig. 1b). This sudden switch of the rotation axis signals an entanglement transition, which is further confirmed by concurrence. The derivative of the concurrence with respect

to η exhibits a discontinuity at the EP, jumping from 1 to 0. Due to the entangled nature of the eigenstates, the system, initially in the product state $|e, n-1\rangle$, evolves into an entangled state after a time t , given by

$$|\psi(t)\rangle = \mathcal{N}_n \{ [2E_G \cos(E_G t/2) + \kappa \sin(E_G t/2)] |e, n-1\rangle - i4\Omega \sin(E_G t/2) |g, n\rangle \}. \quad (4)$$

By measuring the output states after different evolution times, we can extract the information of both the energy gap and the eigenstates. It should be noted that the decaying resonator plays a radically differing role from the ancilla used in the previous experiments [34-37], which was introduced as an artificially engineered environment to the test qubit, but whose dynamics was not included in the effective NH Hamiltonian dynamics. In distinct contrast, in the present system the degree of freedom of R constitutes a part of the Hamiltonian, whose non-Hermitian term is induced by the natural environment.

The experimental demonstration of the non-Hermitian dynamics involves a frequency-tunable superconducting qubit Q and a decaying resonator R with a fixed frequency $\omega_r/2\pi = 6.66$ GHz. Q has an energy decaying rate $\kappa_q \simeq 0.07$ MHz, which is negligible when compared to R 's dissipative rate $\kappa = 5$ MHz. However, Q is highly detuned from R even at its accessible maximum $|e\rangle$ - $|g\rangle$ energy difference $\omega_m = 2\pi \times 6.01$ GHz, with the detuning much larger than their on-resonance swapping coupling $g_r = 2\pi \times 41$ MHz (Fig. 1c). To observe the EP physics, an ac flux is applied to Q , modulating its energy gap as $\omega_q = \omega_0 + \varepsilon \cos(\nu t)$, where ω_0 is the mean $|e\rangle$ - $|g\rangle$ energy difference, and ε and ν denote the modulating amplitude and frequency. This modulation enables Q to interact with R at a preset sideband, with the photon swapping rate Ω tunable by ε (see Supplementary Material).

Before the experiment, the system is initialized to the ground state $|g, 0\rangle$. The experiment starts by transforming Q from the ground state $|g\rangle$ to the excited state $|e\rangle$ with a π pulse, following which the parametric modulation is applied to Q to initiate the Q - R interaction (Fig. 1d). After the modulating pulse, the Q - R state is measured with the assistance of an ancilla qubit (Q_a) and a bus resonator (R_b), which is coupled to both Q and Q_a . The subsequent $Q \rightarrow R_b$, $R_b \rightarrow Q_a$, and $R \rightarrow Q$ quantum state transferring operations map the Q - R state to the Q_a - Q system, whose output state is equivalent to the Q - R state before mapping up to a correction for the dissipation-induced state distortion during the mapping (see Supplementary Material). We note that the Q - Q_a state mapping can be realized in a more direct way with an architecture where the qubits are coupled without employing the bus resonator [41].

The population evolutions coinciding with the NH Hamiltonian dynamics is post-selected by discarding the joint Q_a - Q detection events $|g, g\rangle$. Fig. 2a shows the measured vacuum Rabi oscillation for different values of the rescaled effective coupling strength η , characterized by the population of $|e, 0\rangle$, $P_{e,0}$, as a function of η and the Q - R interaction time. The results clearly show that both the shapes and periods of vacuum Rabi oscillations are significantly modulated by the NH term around the EP $\eta = 1$, where incoherent dissipation is comparable to the coherent interaction. These experimental results are in good agreement with numerical simulations (see Supplementary Material).

To unambiguously confirm the system's quantum behavior, we perform joint Q_a - Q state tomography after the state transfer. To extract full information of the two-qubit entangled state, it is necessary to individually measure all three Bloch vectors for each qubit, and then correlate the results for the two qubits. The z -component can be directly measured by state readout, while measurements of the x - and y -components require y -rotations and x -rotations before state readout, which breaks down excitation-number conservation, and renders it impossible to distinguish individual jump events from no-jump ones. We circumvent this problem by first reconstructing the two-qubit density matrix using all the measurement outcomes, and then discarding the matrix elements associated with $|g, g\rangle$. This effectively post-casts the two-qubit state to the subspace $\{|e, g\rangle, |g, e\rangle\}$. The concurrence associated with the projected density matrix reveals the entanglement between the test qubit and the resonator governed by the NH Hamiltonian. In Fig. 2b, we present the Q - R concurrence inferred in this way, as a function of the rescaled coupling η and interaction time t . To show the entanglement behaviors more clearly, we present the concurrence evolutions for $\eta = 5$ and 0.5 in Fig. 2c and d, respectively. The results demonstrate that the entanglement exhibits distinct evolution patterns in these regimes, featuring under- and over-damping oscillations, respectively.

To reveal the close relation between the exceptional entanglement behavior and the EP, we infer the eigenvalues and eigenstates of the NH Hamiltonian from the output states, measured for different evolution times. The concurrences associated with the two eigenstates, obtained for different values of η , are shown in Fig. 3a and b (dots), respectively. As expected, each of these entanglements exhibits a linear scaling below the EP, where it is saturated and no longer dependent upon η once crossing the EP. The singular features around the EP are manifested by their derivatives to η , which are shown in the insets. The discontinuity of these derivatives at the EP demonstrates that the entanglement behavior is non-analytic at the EP, indicating the occurrence of an entanglement transition. Such a behavior, as a consequence of the competition between the coherent coupling and incoherent dissipation, represents a unique character of strongly correlated NH systems, but has not been reported so far. The unique NH behaviors can also be characterized by the relative phase difference between $|\Phi_{\pm}\rangle$, defined as $\varphi = \varphi_+ - \varphi_-$, with φ_{\pm} representing the relative phases between $|g, 1\rangle$ and $|e, 0\rangle$ in the eigenstates $|\Phi_{\pm}\rangle$. Such a phase difference, inferred from different values of η , is displayed in Fig. 3c, which reflects a transition of the transverse separation between the two maximally entangled

eigenstates at the EP, where $|\Phi_{-}\rangle$ suddenly moves towards the singlet state, while the $|\Phi_{+}\rangle$ towards to one of the triplets. We note that such an exceptional entanglement transition originates from the non-Hermiticity of the Hamiltonian, and is absent in Hermitian qubit-photon systems [42-45].

The real and imaginary parts of the extracted quantum Rabi splitting E_G are shown in Fig. 3d. As theoretically predicted, above the EP the two eigenenergies have a real gap, which is continuously narrowed when the control parameter η is decreased. After crossing the EP, the two levels are re-split but with an imaginary gap, which increases when η is decreased. This corresponds to the real-to-imaginary transition of the vacuum Rabi splitting between the Q - R entangled eigenstates, which is in distinct contrast with the previous experiments on \mathcal{PT} symmetry breaking [29-39], realized with semiclassical Rabi models, where the exceptional physics has no relation with quantum entanglement.

The other important feature associated with the system state evolution is that even a tiny variation of the coupling strength can lead to a significant variation of the NH Hamiltonian dynamics, which is useful for signal amplification in sensing. EP-enhanced sensing protocols have been demonstrated in classical optical systems with artificially engineered gain-and-loss channels [24,25], and demonstrated with single photons in a recent experiment [26], but where no specific physical quantity was estimated. Owing to the eigenstate coalescence at the EP, it remains an open question whether or not an EP-based sensor can achieve a higher signal-to-noise ratio compared to its Hermitian counterpart within the same data acquisition time [46-48], which is beyond the scope of the present study. We here focus on the exploitation of the naturally-occurring dissipation, which is one of the main negative factors restricting the performance of conventional quantum sensing protocols [49,50]. The U(1) symmetry of our system renders it possible to turn this inevitable decoherence effect into a favorable resource for amplifying a weak signal.

In our quantum sensing protocol, the signal is encoded in the vacuum Rabi splitting E_G . The derivative of E_G to the effective Q - R coupling, Ω , is given by

$$dE_G/d\Omega = 2\Omega(\Omega^2 - \kappa^2/16)^{-1/2}, \quad (5)$$

which exhibits a divergent behavior at the EP $\Omega_0 = \kappa/4$. This implies E_G serves as a sensitive indicator for estimating a slight deviation of Ω from Ω_0 , defined as $\Delta\Omega = \Omega - \Omega_0$. The non-Hermiticity-enabled sensitivity enhancement can be characterized by $\mathcal{S} = |\Delta E_G/\Delta\Omega|$ [25]. Fig. 4a displays \mathcal{S} as a function of $\Delta\Omega$, where the data at each point is related to the measured E_G by $\mathcal{S} = (\text{Re } E_G - \text{Im } E_G)/\Delta\Omega$. We extract the functional form of \mathcal{S} in the vicinity of the EP by fitting the experimental data (small gray dots) to the power law function $\mathcal{S} = A|\Delta\Omega/\Omega_0|^B$. The obtained parameter values for $\Delta\Omega > 0$ are $A = 3.192$ and $B = -0.455$, while for $\Delta\Omega < 0$ they are $A = 2.415$ and $B = -0.541$.

The negativity of \mathcal{S} of the marked dot is due to the improper calibration of Ω , which is not used in the fitting (solid line). Within the small regime near the EP, the experimentally measured $|E_G|$ well agrees with the theoretical calculation $|2\sqrt{2\Omega_0\Delta\Omega}|$ (see Supplementary Material), further affirming that E_G exhibits a square-root behavior as a function of the deviation $\Delta\Omega$ around the EP. To further confirm the validity of the protocol, we use the measured data of E_G to calculate $\Delta\Omega$ by

$$\Delta\Omega = \sqrt{E_G^2/4 + \kappa^2/16} - \kappa/4. \quad (6)$$

The dots in Fig. 4b denote thus-inferred deviations, while the stars represent the pre-calibrated values. The NH quantum sensing protocol manifests its superiority within a small region around the EP, exemplified by the point closest to the origin. At this point, the observed under-damping oscillation signal indicates the system works above the EP with $\Delta\Omega = 0.0056$ MHz, which, however, was unreasonably estimated to be $\Delta\Omega = -0.0091$ MHz in the pre-calibration.

The NH quantum sensor works only when the modulating-flux-induced sideband coupling is within a small regime around $\kappa/4$. This restriction can be overcome with a deliberately designed and fabricated architecture involving many qubits [41], each individually coupled to a readout resonator. Different qubits have different on-resonance coupling strengths with their readout resonators. With such a device, a general field can be estimated in two steps. In the first step, a rough estimation is made by parametrically coupling one of these qubits to its readout resonator and observing the Rabi signals. A higher-precision measurement can be performed by encoding the signal field to the sideband interaction of a suitable qubit with its resonator, which occurs near the EP.

In conclusion, we have disclosed an exceptional entanglement transition in a fundamental light-matter system governed by an NH Hamiltonian, establishing a close connection between quantum correlations and non-Hermitian effects. The experimental demonstration is performed in a circuit, where a superconducting qubit is controllably coupled to a resonator with a non-negligible dissipation induced by a natural Markovian reservoir. The quantum signatures are inferred from the conditional output state trajectory, reconstructed by a density-matrix post-projecting method, which enables the extraction of the U(1)-symmetric signal from the noisy background. The results demonstrate that the exceptional entanglement behavior coincides with the real-imaginary shift of the quantum Rabi splitting. This behavior is universal for a variety of dissipative quantum-mechanically correlated systems, e.g., a system composed of two or more coupled qubits with unbalanced decaying rates (see Supplementary Material). We further demonstrate

a quantum sensing protocol by mapping the signal to the vacuum Rabi splitting of the qubit-resonator system under the NH Hamiltonian. Our results pave the way to explore exceptional entanglement phenomena in quantum many-body systems, and open the door to leverage the ubiquitous but stable Markovian reservoir as a useful resource for enhancing quantum sensing.

Acknowledgments: We thank Liang Jiang at University of Chicago for valuable comments. **Funding:** This work was supported by the National Natural Science Foundation of China (Grant No. 11874114, No. 11875108, No. 12204105, No. 11774058, No. 12174058, No. 11974331, No. 11934018, No. 92065114, and No. T2121001), Innovation Program for Quantum Science and Technology (Grant No. 2021ZD0300200), the Strategic Priority Research Program of Chinese Academy of Sciences (Grant No. XDB28000000), the National Key R&D Program under (Grant No. 2017YFA0304100), the Key-Area Research and Development Program of Guangdong Province, China (Grant No. 2020B0303030001), Beijing Natural Science Foundation (Grant No. Z200009), and the Project from Fuzhou University (Grant No. 049050011050).

Author contributions: S.B.Z. predicted the exceptional entanglement transition and conceived the experiment. P.R.H. and X.J.H., supervised by Z.B.Y. and S.B.Z., carried out the experiment. F.W., P.R.H., Z.B.Y., and J.W. analyzed the data. S.B.Z., J.W., Z.B.Y., and W.Y. cowrote the paper. All authors contributed to the interpretation of observed phenomena and helped to improve the presentation of the paper.

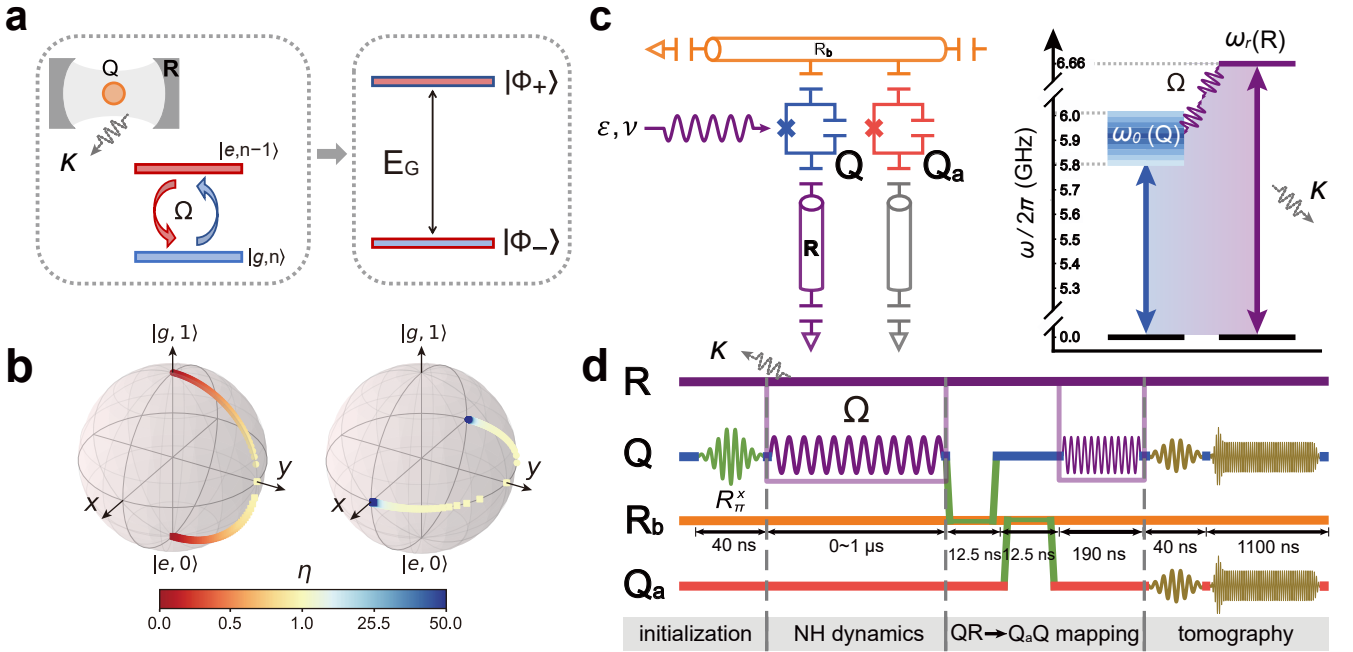


FIG. 1: NH Light-matter interaction and experimental implementation. (a) Theoretical model. The system under investigation involves a quantized field mode with a decaying rate κ resonantly interacting with a matter qubit with a negligible decaying rate. Their interaction is characterized by a coupling strength of Ω . The system's dynamics can be cast onto different $U(1)$ -symmetric eigenspaces, denoted as $\{|e, n-1\rangle, |g, n\rangle\}$, within each of which there exist two eigenstates $|\Phi_\pm\rangle$, separated by a gap of E_G . (b) Bloch representation of $|\Phi_\pm\rangle$ in the single-excitation subspace ($n=1$). For clarity, we here pictorially display the dependence of $|\Phi_\pm\rangle$ on the rescaled coupling strength $\eta = 4\Omega/\kappa$. For $\eta=0$, $|\Phi_\pm\rangle$ correspond to $|e, 0\rangle$ and $|g, 1\rangle$, respectively. With the increase of η , $|\Phi_\pm\rangle$ are respectively rotated around $\pm x$ axes, and merged to the y axis at the EP $\eta=1$, featuring the occurrence of the maximally entangled state $|Y\rangle = (|g, 1\rangle - i|e, 0\rangle)/\sqrt{2}$. After crossing the EP, the eigenvectors $|\Phi_\pm\rangle$ remain on the equatorial plane, but are rotated around the z and $-z$ axes, progressively aligned with the $\pm x$ axes, tending to $|\pm X\rangle = (|g, 1\rangle \pm |e, 0\rangle)/\sqrt{2}$, respectively. (c) Implementation of the NH Hamiltonian. In the experimental system, a superconducting qubit Q is highly detuned from the lossy resonator R with a fixed frequency $\omega_r/2\pi = 6.66$ GHz. The Q - R interaction is enabled with an ac flux, which modulates Q 's energy gap around the mean value $\omega_0(Q)$, with a frequency ν , mediating a photonic swapping coupling at one sideband, with the coupling strength controlled by the modulating amplitude ε . (d) Pulse sequence. The NH dynamics starts with the initial state $|e, 0\rangle$, prepared from $|g, 0\rangle$ with a π pulse. After a preset evolution time, the parametric modulation is switched off, followed by the state mappings $Q \rightarrow R_b$, $R \rightarrow Q$, and $R_b \rightarrow Q_a$, each realized by an on-resonance swapping gate, where Q_a is an ancilla qubit, and R_b represents the bus resonator coupled to both qubits. After these mappings, the Q - R output state produced by the NH dynamics is encoded in the joint Q_a - Q state, which is then measured by quantum state tomography.

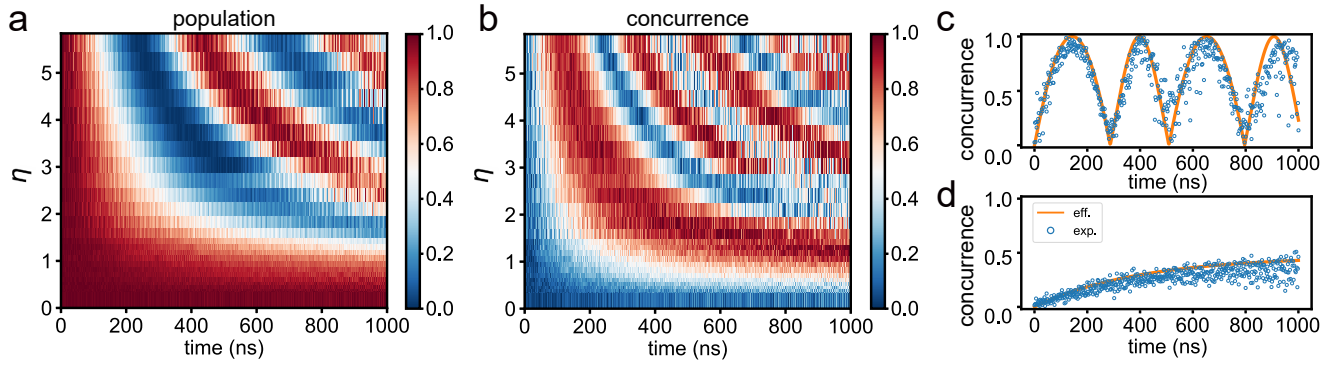


FIG. 2: **Characterization of NH dynamical evolutions.** (a) Measured evolutions of the population $|e, 0\rangle$ for different values of the rescaled coupling η . The signals are extracted by correlating the measurement outcomes of Q and Q_a , which correspond to the outputs of R and Q right before the state mappings. The NH Hamiltonian evolution trajectory is post-selected by discarding the detection events $|g, g\rangle$, and renormalizing the remaining outcomes $|g, e\rangle$ and $|e, g\rangle$. (b) Evolutions of the concurrences for different values of η . The concurrence at each point is inferred with the post-projected density matrix, obtained by reconstructing the output Q - Q_a density matrix, projecting the thus-obtained two-qubit state to the reduced subspace with one excitation, and then renormalizing the remaining matrix elements. (c), (d) Concurrence evolutions for $\eta = 5$ (c) and 0.5 (d). The orange solid curves are the numerical simulations using the effective Hamiltonian and the blue circles are the experimental results.

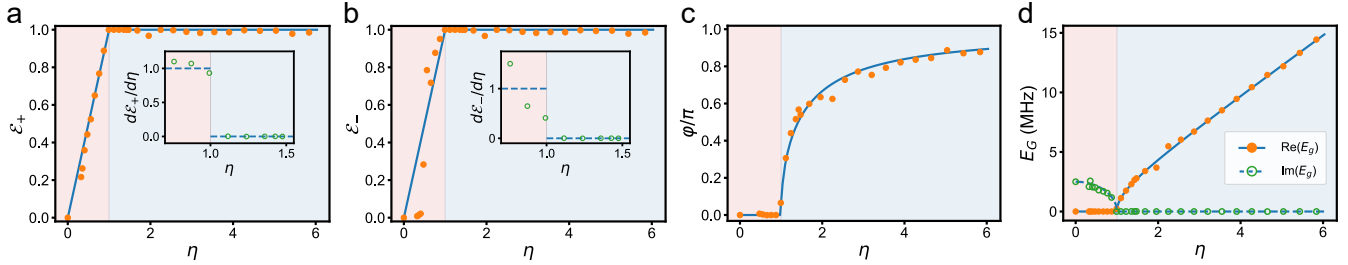


FIG. 3: **Observation of exceptional phase transitions.** (a), (b) Entanglements for the eigenstates $|\Phi_+\rangle$ and $|\Phi_-\rangle$ versus η . We obtain the concurrences \mathcal{E}_\pm at each point based on the corresponding eigenstates, which are mapped out from the Q - R output states, measured for different evolution times. The dots denote the inferred concurrences, which well agree with the results for the ideal output states. The derivatives $d\mathcal{E}_\pm/d\eta$ around the EP, obtained by $[\mathcal{E}_\pm(\eta + \delta\eta) - \mathcal{E}_\pm(\eta)]/\delta\eta$, is displayed in the insets. (c) Relative phase difference (φ) between $|\Phi_\pm\rangle$. This phase difference is defined as $\varphi = \varphi_+ - \varphi_-$, where φ_\pm are the relative phase between $|g, 1\rangle$ and $|e, 0\rangle$ in the eigenstates $|\Phi_\pm\rangle$. (d) Spectral gap E_G . As the eigenspectrum is possessed by the entangled eigenstates of the Q - R system, this gap corresponds to the vacuum Rabi splitting. The solid and dashed lines denote the real and imaginary parts, respectively.

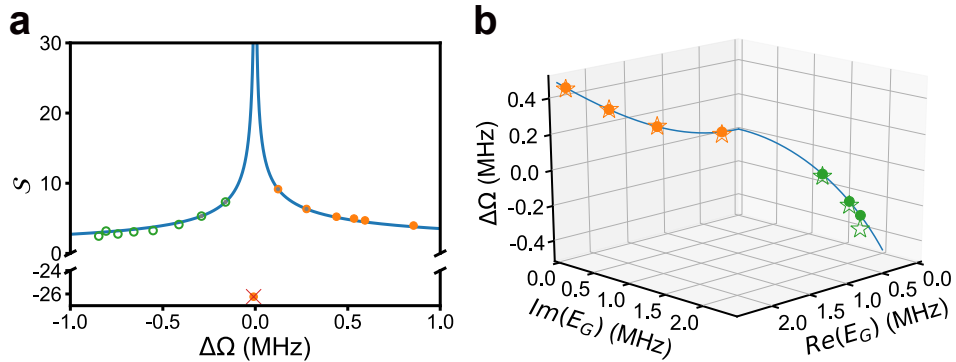


FIG. 4: **Natural-dissipation-enhanced quantum sensing.** (a) Sensitivity enhancement. By encoding the deviation of the effective qubit-resonator coupling from $\Omega_0 = \kappa/4$ in the vacuum Rabi splitting E_G , the signal is amplified by a factor of $S = (\text{Re } E_G - \text{Im } E_G)/\Delta\Omega$. The point marked with “X” is unreasonable owing to the improper calibration of Ω , and thus is unused in the fitting (solid line). (b) Estimated $\Delta\Omega$ versus E_G (dots). The results are calculated by substituting the measured data of E_G into Eq. (6). The stars denote the preset values of $\Delta\Omega$, for which the NH dynamics is observed.

-
- [1] C. M. Bender, S. Boettcher, Real spectra in non-Hermitian Hamiltonians having \mathcal{PT} symmetry. *Phys. Rev. Lett.* **80**, 5243-5246 (1998).
- [2] C. M. Bender, D. C. Brody, H. F. Jones, Complex extension of quantum mechanics. *Phys. Rev. Lett.* **89**, 270401 (2002).
- [3] N. Moiseyev, *Non-Hermitian Quantum Mechanics* (Cambridge Univ. Press, 2011).
- [4] Ş. K. Özdemir, S. Rotter, F. Nori, L. Yang, Parity-time symmetry and exceptional points in photonics, *Nat. Mater.* **18**, 783-798 (2019).
- [5] E. J. Bergholtz, J. C. Budich, F. K. Kunst, Exceptional topology of non-Hermitian systems, *Rev. Mod. Phys.* **93**, 015005 (2021).
- [6] K. Ding, C. Fang, G. Ma, Non-Hermitian topology and exceptional-point geometries, arXiv:2204.11601 (2022).
- [7] Z.-P. Liu, J. Zhang, Ş. K. Özdemir, B. Peng, H. Jing, X.-Y. Lü, C.-W. Li, L. Yang, F. Nori, Y.-X. Liu, Metrology with \mathcal{PT} -symmetric cavities: enhanced sensitivity near the \mathcal{PT} -phase transition. *Phys. Rev. Lett.* **117**, 110802 (2016).
- [8] M. Zhang, W. Sweeney, C. W. Hsu, L. Yang, A. D. Stone, L. Jiang, Quantum noise theory of exceptional point amplifying sensors, *Phys. Rev. Lett.* **123**, 180501 (2019).
- [9] Y. Chu, Y. Liu, H. Liu, J. Cai, Quantum sensing with a single-qubit pseudo-Hermitian system, *Phys. Rev. Lett.* **124**, 020501 (2020).
- [10] X.-W. Luo, C. Zhang, S. Du, Quantum squeezing and sensing with pseudo anti-parity-time symmetry, *Phys. Rev. Lett.* **128**, 173602 (2022).
- [11] J. Wang, D. Mukhopadhyay, G. S. Agarwal, Quantum Fisher information perspective on sensing in anti-PT symmetric systems, *Phys. Rev. Res.* **4**, 013131 (2022).
- [12] C. Dembowski, H.-D. Gräf, H. L. Harney, A. Heine, W. D. Heiss, H. Rehfeld, A. Richter, Experimental observation of the topological structure of exceptional points. *Phys. Rev. Lett.* **86**, 787-790 (2001).
- [13] Y. Choi, S. Kang, S. Lim, W. Kim, J.-R. Kim, J.-H. Lee, K. An, Quasieigenstate coalescence in an atom-cavity quantum composite. *Phys. Rev. Lett.* **104**, 153601 (2010).
- [14] T. Gao, E. Estrecho, K. Y. Bliokh, T. C. H. Liew, M. D. Fraser, S. Brodbeck, M. Kamp, C. Schneider, S. Höfling, Y. Yamamoto, F. Nori, Y. S. Kivshar, A. G. Truscott, R. G. Dall, E. A. Ostrovskaya, Observation of non-Hermitian degeneracies in a chaotic exciton-polariton billiard. *Nature* **526**, 554-558 (2015).
- [15] D. Zhang, X.-Q. Luo, Y.-P. Wang, T.-F. Li, J. Q. You, Observation of the exceptional point in cavity magnon-polaritons. *Nat. Commun.* **8**, 1368 (2017).
- [16] F. E. Öztürk, T. Lappe, G. Hellmann, J. Schmitt, J. Klaers, F. Vewinger, Observation of a non-Hermitian phase transition in an optical quantum gas, *Science* **372**, 88-91 (2021).
- [17] W. Tang, X. Jiang, K. Ding, Y.-X. Xiao, Z.-Q. Zhang, C. T. Chan, G. Ma, Exceptional nexus with a hybrid topological invariant. *Science* **370**, 1077-1080 (2020).
- [18] K. Wang, A. Dutt, K. Y. Yang, C. C. Wojcik, J. Vučković, S. Fan, Generating arbitrary topological windings of a non-Hermitian band. *Science* **371**, 1240-1245 (2021).
- [19] K. Wang, A. Dutt, C. C. Wojcik, S. Fan, Topological complex-energy braiding of non-Hermitian bands. *Nature* **598**, 59-64 (2021).
- [20] Y. S. S. Patil, J. H'oller, P. A. Henry, C. Guria, Y. Zhang, L. Jiang, N. Kralj, N. Read, J. G. E. Harris, Measuring the knot of non-Hermitian degeneracies and non-commuting braids, *Nature* **607**, 271-275 (2022).
- [21] J. Doppler, A. A. Mailybaev, J. Böhm, U. Kuhl, A. Girschik, F. Libisch, T. J. Milburn, P. Rabl, N. Moiseyev, S. Rotter, Dynamically encircling an exceptional point for asymmetric mode switching. *Nature* **537**, 76-79 (2016).
- [22] H. Xu, D. Mason, L. Jiang, J. G. E. Harris, Topological energy transfer in an optomechanical system with exceptional points. *Nature* **537**, 80-83 (2016).
- [23] J. W. Yoon, Y. Choi, C. Hahn, G. Kim, S. H. Song, K.-Y. Yang, J. Y. Lee, Y. Kim, C. S. Lee, J. K. Shin, H.-S. Lee, P. Berini, Time-asymmetric loop around an exceptional point over the full optical communication band. *Nature* **562**, 86-90 (2018).
- [24] W. Chen, Ş. K. Özdemir, G. Zhao, J. Wiersig, L. Yang, Exceptional points enhance sensing in an optical microcavity, *Nature* **548**, 192-196 (2017).
- [25] H. Hodaie, A. U. Hassan, S. Wittek, H. Garcia-Gracia, R. El-Ganainy, D. N. Christodoulides, M. Khajavikhan, Enhanced sensitivity at higher-order exceptional points, *Nature* **548**, 187-191 (2017).
- [26] S. Yu, Y. Meng, J.-S. Tang, X.-Y. Xu, Y.-T. Wang, P. Yin, Z.-J. Ke, W. Liu, Z.-P. Li, Y.-Z. Yang, G. Chen, Y.-J. Han, C.-F. Li, G.-C. Guo, Experimental investigation of quantum \mathcal{PT} -enhanced sensor, *Phys. Rev. Lett.* **125**, 240506 (2020).
- [27] K. Wang, L. Xiao, J. C. Budich, W. Yi, P. Xue, Simulating exceptional non-Hermitian metals with single-photon interferometry, *Phys. Rev. Lett.* **127**, 026404 (2021).
- [28] Y.-L. Fang, J.-L. Zhao, Y. Zhang, D.-X. Chen, Q.-C. Wu, Y.-H. Zhou, C.-P. Yang, F. Nori, Experimental demonstration of coherence flow in PT- and anti-PT-symmetric systems, *Commun. Phys.* **4**, 223 (2021).
- [29] P. Peng, W. Cao, C. Shen, W. Qu, J. Wen, L. Jiang, Y. Xiao, Anti-parity-time symmetry with flying atoms, *Nat. Phys.* **12**, 1139-1145 (2016).
- [30] J. Li, A. K. Harter, J. Liu, L. d. Melo, Y. N. Joglekar, L. Luo, Observation of parity-time symmetry breaking transitions in a dissipative Floquet system of ultracold atoms, *Nat. Commun.* **10**, 855 (2019).
- [31] Z. Ren, D. Liu, E. Zhao, C. He, K. K. Pak, J. Li, G.-B. Jo, Chiral control of quantum states in non-Hermitian spin-orbit-

- coupled fermions, *Nat. Phys.* **18**, 385-389 (2022).
- [32] W.-C. Wang, Y.-L. Zhou, H.-L. Zhang, J. Zhang, M.-C. Zhang, Y. Xie, C.-W. Wu, T. Chen, B.-Q. Ou, W. Wu, H. Jing, P.-X. Chen, Observation of \mathcal{PT} -symmetric quantum coherence in a single-ion system, *Phys. Rev. A* **103**, L020201 (2021).
- [33] L. Ding, K. Shi, Q. Zhang, D. Shen, X. Zhang, W. Zhang, Experimental determination of \mathcal{PT} -symmetric exceptional points in a single trapped ion, *Phys. Rev. Lett.* **126**, 083604 (2021).
- [34] Y. Wu, W. Liu, J. Geng, X. Song, X. Ye, C. K. Duan, X. Rong, J. F. Du, Observation of parity-time symmetry breaking in a single-spin system. *Science* **364**, 878-880 (2019).
- [35] W. Liu, Y. Wu, C.-K. Duan, X. Rong, J. Du, Dynamically encircling an exceptional point in a real quantum system, *Phys. Rev. Lett.* **126**, 170506 (2021).
- [36] W. Zhang, X. Ouyang, X. Huang, X. Wang, H. Zhang, Y. Yu, X. Chang, Y. Liu, D.-L. Deng, and L.-M. Duan, Observation of non-Hermitian topology with nonunitary dynamics of solid-state spins, *Phys. Rev. Lett.* **127**, 090501 (2021).
- [37] S. Dogra, A. A. Melnikov, G. S. Paraoanu, Quantum simulation of parity-time symmetry breaking with a superconducting quantum processor, *Commun. Phys.* **4**, 26 (2021).
- [38] M. Naghiloo, M. Abbasi, Y. N. Joglekar, K. W. Murch, Quantum state tomography across the exceptional point in a single dissipative qubit. *Nat. Phys.* **15**, 1232-1236 (2019).
- [39] Z. Wang, Z. Xiang, T. Liu, X. Song, P. Song, X. Guo, L. Su, H. Zhang, Y. Du, D. Zheng, Observation of the exceptional point in superconducting qubit with dissipation controlled by parametric modulation, *Chin. Phys. B* **30**, 100309 (2021).
- [40] W. K. Wootters, Entanglement of formation of an arbitrary state of two qubits, *Phys. Rev. Lett.* **80**, 2245-2248 (1998).
- [41] S. Xu, Z.-Z. Sun, K. Wang, L. Xiang, Z. Bao, Z. Zhu, F. Shen, Z. Song, P. Zhang, W. Ren, X. Zhang, H. Dong, J. Deng, J. Chen, Y. Wu, Z. Tan, Y. Gao, F. Jin, X. Zhu, C. Zhang, N. Wang, Y. Zou, J. Zhong, A. Zhang, W. Li, W. Jiang, L.-W. Yu, Y. Yao, Z. Wang, H. Li, Q. Guo, C. Song, H. Wang, D.-L. Deng, Digital simulation of non-Abelian anyons with 68 programmable superconducting qubits, arXiv:2211.09802 (2022).
- [42] R. J. Thompson, G. Rempe, H. J. Kimble, Observation of normal-mode splitting for an atom in an optical cavity, *Phys. Rev. Lett.* **68**, 1132-1135 (1992).
- [43] F. Bernardot, P. Nussenzveig, M. Brune, J. M. Raimond, S. Haroche, Vacuum Rabi splitting observed on a microscopic atomic sample in a microwave cavity, *Europhys. Lett.* **17**, 33 (1992).
- [44] J. M. Fink, M. Goppl, M. Baur, R. Bianchetti, P. J. Leek, A. Blais, A. Wallraff, Climbing the Jaynes-Cummings ladder and observing its nonlinearity in a cavity QED system, *Nature* **454**, 315-318 (2008).
- [45] L. S. Bishop, J. M. Chow, J. Koch, A. A. Houck, M. H. Devoret, E. Thuneberg, S. M. Girvin, R. J. Schoelkopf, Nonlinear response of the vacuum Rabi resonance, *Nat. Phys.* **5**, 105-109 (2009).
- [46] H.-K. Lau, A. A. Clerk, Fundamental limits and non-reciprocal approaches in non-Hermitian quantum sensing, *Nat Commun.* **9**, 4320 (2018).
- [47] W. Langbein, No exceptional precision of exceptional-point sensors, *Phys. Rev. A* **98**, 023805 (2018).
- [48] C. Chen, L. Jin, R.-B. Liu, Sensitivity of parameter estimation near the exceptional point of a non-Hermitian system, *New J. Phys.* **21**, 083002 (2019).
- [49] C. L. Degen, F. Reinhard, P. Cappellaro, Quantum sensing, *Rev. Mod. Phys.* **89**, 035002 (2017).
- [50] L. Pezzè, A. Smerzi, M. K. Oberthaler, R. Schmied, P. Treutlein, Quantum metrology with nonclassical states of atomic ensembles, *Rev. Mod. Phys.* **90**, 035005 (2018).
- [51] S.-B. Zheng, G.-C. Guo, Efficient scheme for two-atom entanglement and quantum information processing in cavity QED, *Phys. Rev. Lett.* **85**, 2392-2395 (2000).
- [52] S. Osnaghi, P. Bertet, A. Auffeves, P. Maioli, M. Brune, J. M. Raimond, S. Haroche, Coherent control of an atomic collision in a cavity, *Phys. Rev. Lett.* **87**, 037902 (2001).
- [53] C. Song, K. Xu, W. Liu, C.-P. Yang, S.-B. Zheng, H. Deng, Q. Xie, K. Huang, Q. Guo, L. Zhang, P. Zhang, D. Xu, D. Zheng, X. Zhu, H. Wang, Y.-A. Chen, C.-Y. Lu, S. Han, J.-W. Pan, 10-qubit entanglement and parallel logic operations with a superconducting circuit, *Phys. Rev. Lett.* **119**, 180511 (2017).
- [54] Y. Zhou, Z. Zhang, Z. Yin, S. Huai, X. Gu, X. Xu, J. Allcock, F. Liu, G. Xi, Q. Yu, H. Zhang, M. Zhang, H. Li, X. Song, Z. Wang, D. Zheng, S. An, Y. Zheng, S. Zhang, Rapid and unconditional parametric reset protocol for tunable superconducting qubits, *Nat. Commun.* **12**, 5924 (2021).

Supplementary Materials for “Exceptional entanglement transition and natural-dissipation-enhanced quantum sensing”

Peirong Han^{1,*} Fan Wu^{1,*} Xinjie Huang^{1,*} Huaizhi Wu¹, Chang-Ling Zou^{2,3,8},
Wei Yi^{2,3,8}, Mengzhen Zhang⁴, Hekang Li⁵, Kai Xu^{5,6,8}, Dongning Zheng^{5,6,8},
Heng Fan^{5,6,8}, Jianming Wen^{7,†} Zhenbiao Yang^{1,8,‡} and Shibiao Zheng^{1,8§}

¹*Department of Physics, Fuzhou University, Fuzhou, Fujian,
350108, China*

²*CAS Key Laboratory of Quantum Information,
University of Science and
Technology of China, Hefei 230026, China*

³*CAS Center for Excellence in Quantum Information and Quantum Physics,
University of Science and Technology of China,
Hefei 230026, China*

⁴*Pritzker School of Molecular Engineering,
University of Chicago,
Chicago, IL 60637, USA*

⁵*Institute of Physics,
Chinese Academy of Sciences, Beijing 100190,
China*

⁶*CAS Center for Excellence in Topological Quantum Computation,
University of Chinese Academy of Sciences,
Beijing 100190, China*

⁷*Department of Physics,
Kennesaw State University, Marietta, Georgia
30060, USA*

⁸*Hefei National Laboratory, Hefei 230088, China*

Contents

1. Experimental setup and system parameters	2
2. Controlled Q-R sideband couplings	2
3. Numerical simulations of the non-Hermitian Hamiltonian dynamics	5
4. Joint Q-R quantum state tomography	6
5. Qubit readout corrections	7
6. Extraction of eigenenergies and eigenstates of the non-Hermitian Hamiltonian	8
7. Performance of the natural-dissipation-enhanced quantum sensing	9
8. Exceptional entanglement transition in a two-qubit system	10

*These authors contribute equally to this work.

†E-mail: jianming.wen@kennesaw.edu

‡E-mail: zbyangmk@gmail.com

§E-mail: fqiqo@fzu.edu.cn

1. EXPERIMENTAL SETUP AND SYSTEM PARAMETERS

Our device consists of five frequency-tunable superconducting Xmon qubits, labeled as Q_j ($j=1$ to 5), each with an anharmonicity of approximately $2\pi \times 240$ MHz. Every Xmon qubit has a microwave line (XY line) to drive its state transitions and an individual flux line (Z line) to dynamically tune its frequency. These two constituents consequently make each qubit flexibly on-and-off coupled (with a coupling strength $g_{b,j}$) to a bus resonator R_b with a bare frequency $\omega_b/2\pi \simeq 5.582$ GHz and an energy relaxation time $T_b \simeq 13$ μ s. Besides, each qubit is also dispersively coupled to its own readout resonator, whose frequency and leakage rate are denoted by $\omega_{r,j}$ and κ_j , respectively. All the readout resonators are coupled to a common transmission line to enable the multiplexed readout of all qubits' states. It is worth pointing out that the readout measurement performed here features both single-shot and quantum nondestructive characteristics, and is achieved with the assistance of an impedance-transformed Josephson parametric amplifier (JPA) with a bandwidth of about 150 MHz. In this experiment, the NH Hamiltonian dynamics is realized by coupling Q_1 to its readout resonator R_1 , and Q_2 serves as an ancilla qubit for reading out the joint Q_1 - R_1 output state. The parameters of Q_j and R_j ($j = 1, 2$) are listed in TABLE S1, including energy relaxation time $T_{1,j}$, Ramsey Gaussian dephasing time $T_{2,j}^*$, and spin echo Gaussian dephasing time $T_{2,j}^{SE}$ at their idle frequency $\omega_{id,j}$. The readout fidelity ($F_{k,j}$) is defined as the probability of correctly reading out the state of Q_j when it is in $|k\rangle$. For simplicity, we will omit the subscript "1" of the test qubit and its readout resonator, and use the subscript "a" to denote the ancilla qubit. The detailed experimental setup, including the whole electronics and wiring for the device control, is summarized in Fig. S1. The readout resonator for Q is painted blue as an emphasis in the figure, as it is also used as a decaying resonator for constructing the desired non-Hermitian dynamics.

Parameters	Q_1 (Q)	Q_2 (Q_a)
Qubit idle frequency, $\omega_{id,j}/2\pi$	5.99 GHz	5.23 GHz
Coupling strength to the bus resonator R_b , $g_{b,j}/2\pi$	20.9 MHz	20.3 MHz
Coupling strength to the decaying resonator R_j , $g_{r,j}/2\pi$	41 MHz	40 MHz
Energy relaxation time, $T_{1,j}$	14.3 μ s	24.8 μ s
Ramsey dephasing time, $T_{2,j}^*$	5.3 μ s	1.1 μ s
Dephasing time with spin echo, $T_{2,j}^{SE}$	14.7 μ s	3.5 μ s
Frequency of decaying resonator, $\omega_{r,j}/2\pi$	6.66 GHz	6.76 GHz
Leakage rate of decaying resonator, κ_j	1/200 ns^{-1}	1/226 ns^{-1}
$ g\rangle$ state readout fidelity, $F_{g,j}$	0.981	0.977
$ e\rangle$ state readout fidelity, $F_{e,j}$	0.901	0.902

TABLE S1: **Parameters of the circuit QED system.** The parameters of both the test qubit (Q_1) and ancilla qubit (Q_2) are measured at their idle frequencies $\omega_{id,j}$ ($j = 1, 2$). $\omega_{id,j}$ is also the point at which the single-qubit rotations and state tomographies are performed. $g_{b,j}$ denotes the R_b - Q_j coupling strength, which was inferred from the quantum Rabi signals of Q_j resonantly coupled to R_b . $g_{r,j}$ is the Q_j - R_j coupling strength, which was deducted by measuring the dispersive frequency shift of the decaying resonator. The fidelity for correctly recording each qubit's state in experiment is $F_{k,j}$, characterized by extracting the state information of each readout resonator with the resonance frequency and leakage rate $\omega_{r,j}$ and κ_j , respectively.

2. CONTROLLED Q - R SIDEBAND COUPLINGS

In a superconducting circuit, the parametric modulation is often achieved by modulating the flux. In our work, the modulation protocol is implemented by applying an external flux of the form

$$\Phi_{ext}(t) = \bar{\Phi} + \tilde{\Phi} \cos(\nu t), \quad (S1)$$

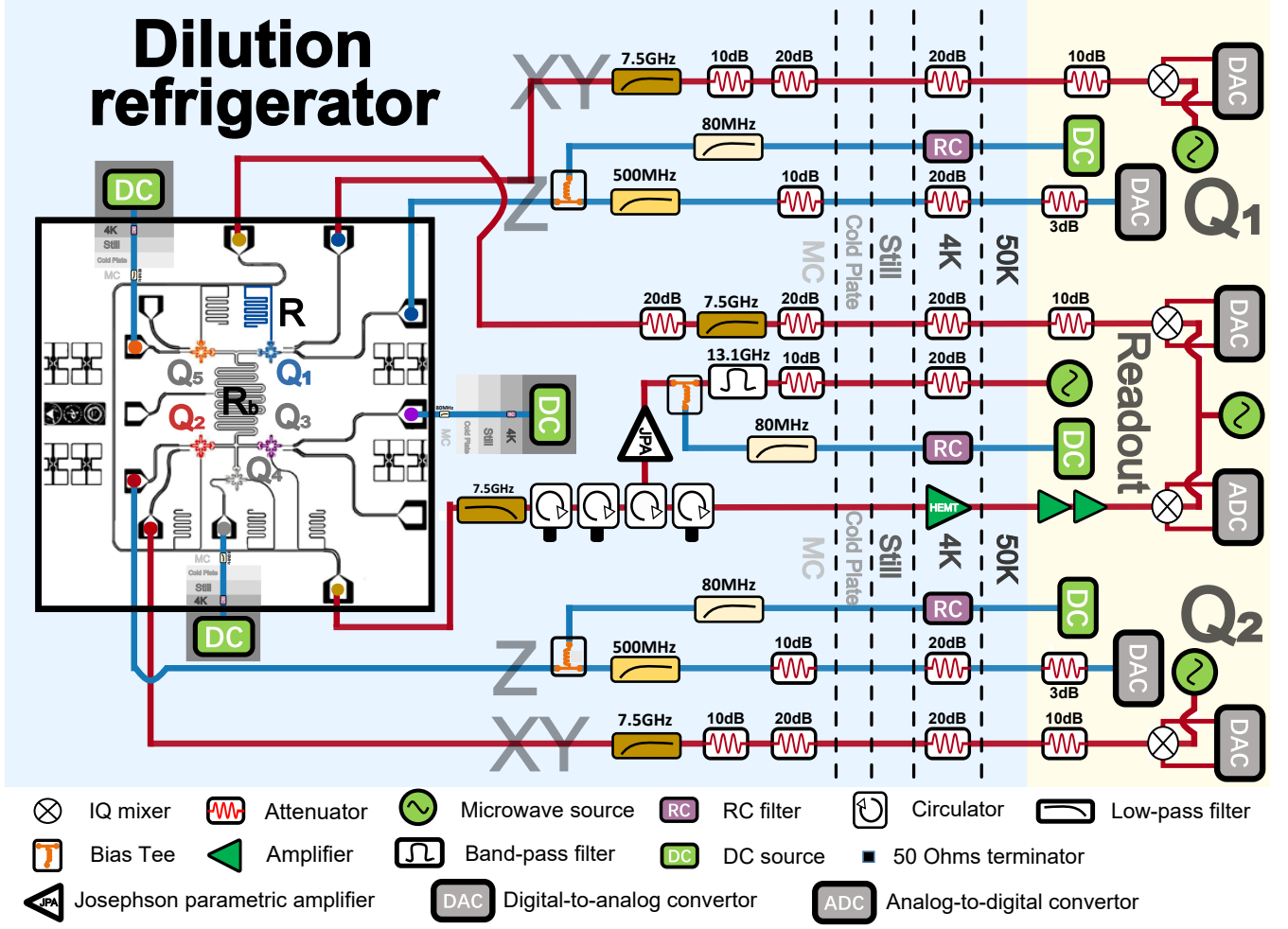


FIG. S1: **Schematic layouts of our circuit QED system and experimental setup.** The superconducting circuit has five frequency-tunable Xmon qubits, labeled from Q_1 to Q_5 . Each qubit can be individually frequency-biased and frequency-modulated (through the Z line) and flipped (through the XY line). Thanks to such flexible adjustability, every qubit can be coupled to the bus resonator (R_b) in a controllable way. The XY control of each qubit is implemented by mixing the low-frequency signals (yielded by two Digital-to-analog converter (DAC)'s I/Q channels) with a Microwave source (MS) at 5.5-GHz carrier frequency; while the Z control is fulfilled by two signals: one is produced by the Direct-current (DC) biasing line from a low frequency DC source, and the other is directly obtained from the Z control of a DAC. Meantime, every qubit has its own readout resonator which helps to project out the state information. Experimentally, this is accomplished by the mixing of the signals of two Analog-to-digital converter (ADC)'s I/Q channels and one MS at about 6.6-GHz frequency to output a readout pulse. Both the employed DAC and ADC are field-programmable-gate-array-controlled and respond at the nanosecond scale. The output from the circuit, before being captured and demodulated by the ADC, is sequentially amplified by an impedance-transformed Josephson parametric amplifier (JPA, which is pumped by a 13.5-GHz MS and modulated by a DC bias), a high electron mobility transistor (HEMT), and two room temperature amplifiers. Furthermore, a few custom-made circulators, attenuators, and filters are utilized at some specific locations of the signal lines to reduce the noise that may affect the operations of the device.

to tune the transition frequency of the superconducting qubit Q . Here, $\bar{\Phi}$ is the parking flux, $\tilde{\Phi}$ and ν' are, respectively, the modulation amplitude and frequency. The Josephson energy of Q is modified through an external flux Φ_{ext} ,

$$E_J(t) = E_J \Sigma \left| \cos \left[\pi \frac{\Phi_{ext}(t)}{\Phi_0} \right] \right|, \quad (\text{S2})$$

with $\Phi_0 = h/(2e)$ being the flux quantum. Under this modification, the transition frequency of Q is modulated as (setting $\hbar = 1$)

$$\omega_e(t) \simeq \sqrt{8E_c E_J(t)} - E_c, \quad (\text{S3})$$

where E_c represents the charge energy. In light of the sinusoidal function in $E_J(t)$ of Eq. (S2), Eq. (S3) can be evaluated by Fourier series expansion, that is,

$$\omega_e(t) = \omega_0 + \sum_{k=1}^{\infty} \varepsilon_k \cos(\omega_k t). \quad (\text{S4})$$

Here, ω_0 stands for the averaged Q transition frequency, and ε_k and ω_k denote the amplitude and frequency of the k -th harmonic, respectively.

Due to the nonlinear flux dependence of $\omega_e(\Phi_{ext})$, the average value ω_0 of the Q transition frequency will be shifted away from $\omega_e(\bar{\Phi})$ by some amount, and this shifted frequency amount can be measured by a Ramsey interferometer. In this experiment, the operation point during the modulation procedure is chosen at the sweet point of Q with $\Phi_{ext} = 0$ and $\bar{\Phi} = 0$. This is because at the Q 's sweet point, Eq. (S4) can be substantially simplified to the following compact expression,

$$\omega_e(t) \approx \omega_0 + \varepsilon \cos(\nu t), \quad (\text{S5})$$

by simply keeping one dominant Fourier component while neglecting all the rest higher-order harmonic terms. Here the actual qubit modulation frequency ν is twice that of the corresponding flux modulation [54]. In the experiment, ε can be readily manipulated by tailoring the z-pulse amplitude (zpa).

Under this parametric modulation, the coherent dynamics of the system combined by Q and R is governed by the Hamiltonian (setting $\hbar = 1$)

$$H = \omega_e(t)|e\rangle\langle e| + \omega_r a^\dagger a + g_r(a^\dagger|g\rangle\langle e| + a|e\rangle\langle g|), \quad (\text{S6})$$

where ω_r is the center frequency of the quantized decaying bosonic mode and g_r ascribes the on-resonance coupling strength between Q and R . Now, substituting Eq. (S5) into Eq. (S6) and working in the interaction picture would transform the full Hamiltonian of Eq. (S6) into

$$H_I = g_r e^{i\Delta_r t - i\mu \sin(\nu t)} a^\dagger |g\rangle\langle e| + H.c., \quad (\text{S7})$$

where $\mu = \varepsilon/\nu$, $\Delta_r = \omega_r - \omega_0$, and $H.c.$ means the Hermitian conjugate. Using the Jacobi-Anger expansion

$$e^{i\mu \sin \theta} = \sum_{-\infty}^{\infty} J_n(\mu) e^{in\theta}, \quad (\text{S8})$$

with $J_n(x)$ being the n -th Bessel function of the first kind, Eq. (S7) then becomes

$$H_I = g_r \left[\sum_{n=-\infty}^{\infty} J_n(\mu) e^{-i(n\nu - \Delta_r)t} a^\dagger |g\rangle\langle e| + H.c. \right]. \quad (\text{S9})$$

Equation (S9) looks complicated and time-dependent. In practice, its complexity and time-dependence can be easily removed under the conditions $\nu = \Delta_r$ ($\nu = \Delta_r/2$) and $g_r \ll \nu$. Accordingly, this frequency setting is referred to as the first-order (or second-order) sideband modulation for establishing the Q - R coupling with the coupling strength $\Omega = J_1(\mu)g_r$ (or $\Omega = J_2(\mu)g_r$). As a consequence, a swap operation of $|e, 0\rangle \leftrightarrow |g, 1\rangle$ is available under such a modulation arrangement.

Without considering the interference of R_b , it is favorable to use the second-order sideband coupling due to the limitation of the available modulating flux. However, when this interaction is weak, it may be strongly intervened by the first-order sideband coupling associated with R_b . To optimize the parametric modulation, we prepare Q in the $|e\rangle$ -state, and observe the output $|e\rangle$ -state population (P_e) after a modulating pulse with a fixed duration of 1 μs . Fig. S2a and Fig. S2b display the populations, measured respectively under the first-order and second-order sideband modulations. Figure S2b shows a crossing region where the qubit Q is effectively coupled to both resonators R and R_b . In this region, the first-order sideband interaction (labeled with "1") with R_b coincides with the second-order sideband interaction (labeled with "2") with R , resulting in undesired effects in our experiments. To circumvent this issue, we use the first-order sideband modulation to realize Q - R swapping interaction for the corresponding region. To confirm the validity of these modulations, in Fig. S2c we present the vacuum Rabi oscillation signals for the test qubit induced by these sideband couplings for different modulating amplitudes. In this way, we arrange our modulation protocol and confine the system's energy-level structure to the configuration shown in Fig. 1 of the main text.

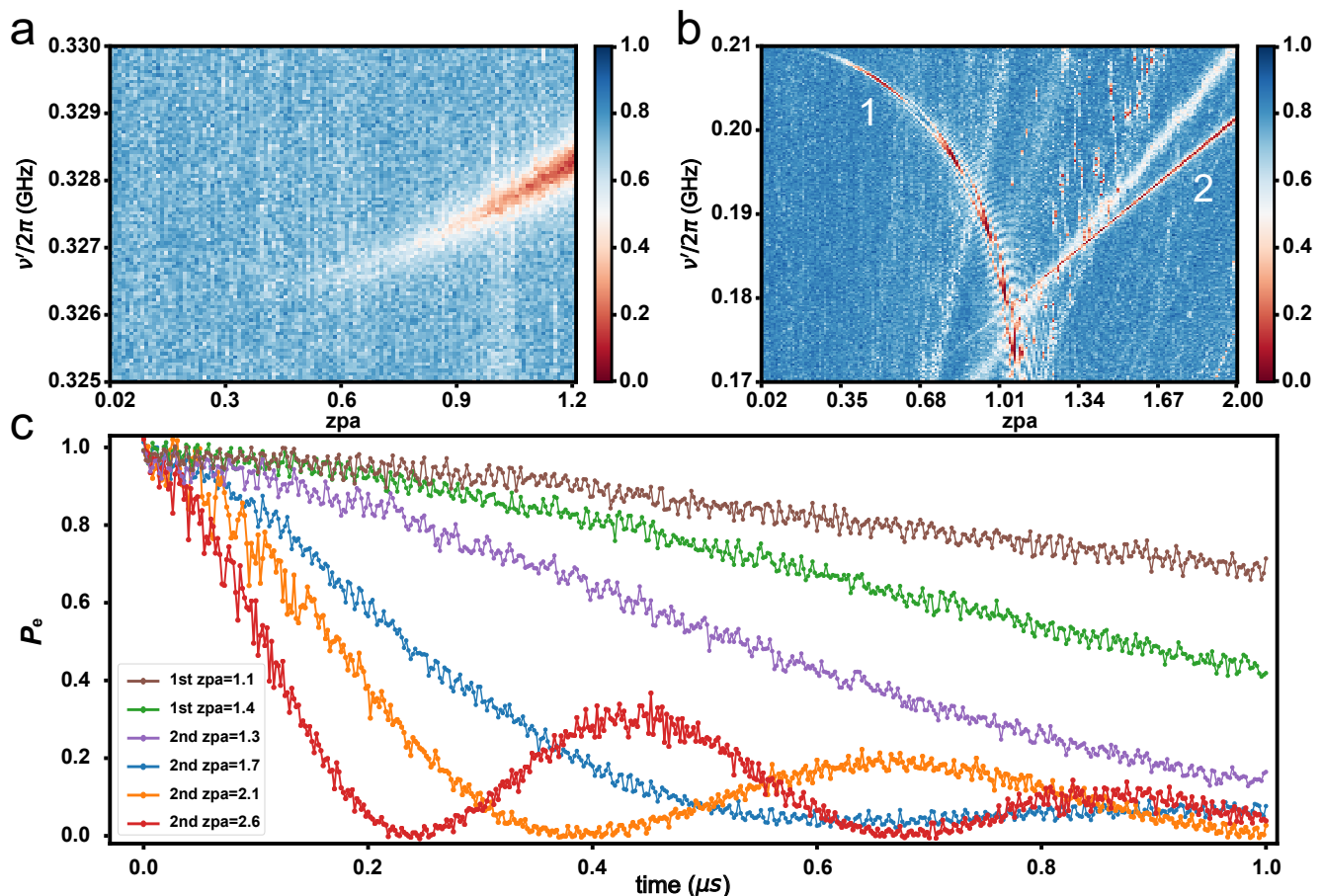


FIG. S2: Scanning map of the population P_e of the superconducting qubit Q after 1- μs parametric modulations. (a) The measured data obtained by coupling Q with R via the first-order sideband modulation. (b) The measured data labeled as “1” (“2”) attained by establishing the Q - R_b (Q - R) interaction via the first-order (second-order) sideband modulation. Here, the x -axis states the modulation amplitude in zpa and the y -axis gives the modulation frequency. (c) Temporal evolution of the population P_e under different single-tone modulations.

3. NUMERICAL SIMULATIONS OF THE NON-HERMITIAN HAMILTONIAN DYNAMICS

To ensure that the system dynamics can be well described by the effective Hamiltonian \mathcal{H}_{NH} in the main text, we have carried out similar calculations using the full Hamiltonian H_I of Eq. (S7) given above. In Fig. S3, we have presented some representative numerical results calculated by these two Hamiltonians for comparison. In these calculations, we have uniformly utilized the Lindblad master equation to compute the temporal evolution of our system (setting $\hbar = 1$),

$$\frac{\partial \rho}{\partial t} = -i[H_I, \rho] + \sum_{k=q,r} \left(L_k \rho L_k^\dagger - \frac{1}{2} \{L_k^\dagger L_k, \rho\} \right), \quad (\text{S10})$$

with the Lindblad dissipators $L_q = \sqrt{\gamma} \sigma^-$ and $L_r = \sqrt{\kappa} a$, the decay rates γ and κ of the qubit and microwave field, and σ^- the spin transition operator. In order to study the behavior of the system within the subspace $\{|g, 1\rangle, |e, 0\rangle\}$, we exploit the post-selection method to effectively eliminate any dynamics outside this subspace. This approach allows us to describe the system’s behavior within this subspace using an effective non-Hermitian Hamiltonian \mathcal{H}_{NH} .

To confirm the validity of the approximations for obtaining the effective Hamiltonian, we perform numerical simulations with the full Hamiltonian. The results are presented in Figs. S3a to f. It is worth noting that the evolution of the entanglement differs significantly from the population dynamics. In addition to the doubled oscillation frequency, the entanglement is much more sensitive to the control parameter. For instance, when the population of state $|g, 1\rangle$ changes from 0 to 0.1, the concurrence increases by an amount ~ 0.6 , which is one order of magnitude larger than the

variation in the population of state $|g, 1\rangle$. Therefore, the concurrence (Figs. S3e and f) is much more influenced by the high-frequency oscillating terms than the population (Fig. S3b and c). In these figures, the orange and blue lines respectively denote the numerical results with the effective and full Hamiltonians, and the circles are the experimental data.

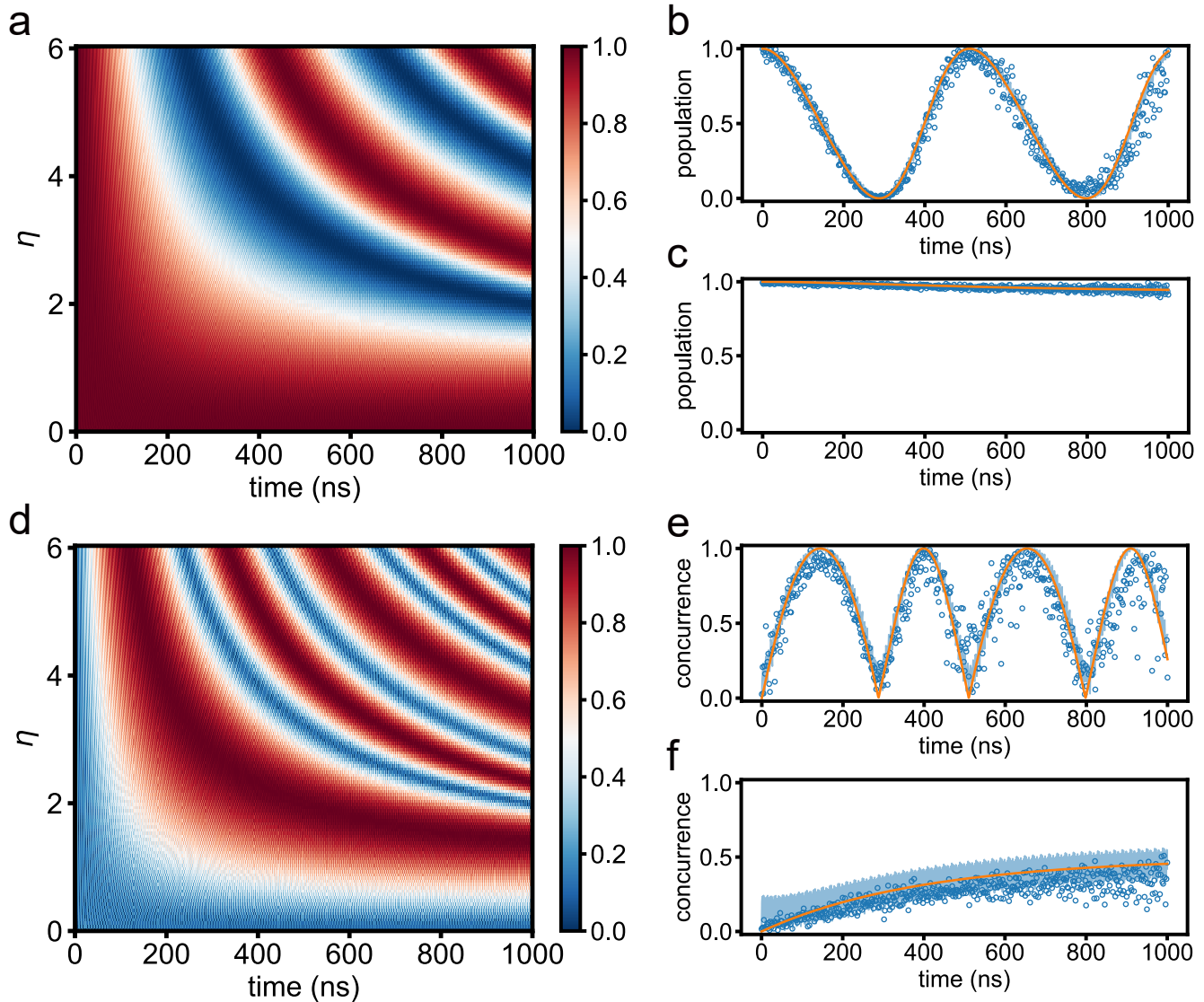


FIG. S3: **Numerical evolutions of the system's non-Hermitian evolution using the full Hamiltonian H_I .** (a) Vacuum Rabi oscillations by calculating $P_{|e,0\rangle}^N$ in terms of the rescaled coupling $\eta = 4\Omega/\kappa$. As an example, (b) and (c) compare $P_{|e,0\rangle}^N$ obtained respectively with use of the full (blue) and effective (orange) Hamiltonians before ($\eta = 5$) and after ($\eta = 0.5$) the exceptional entanglement transition. (d) Concurrence \mathcal{E} evolution for different η . As an example, (e) and (f) compare \mathcal{E} obtained respectively with use of the full (blue) and effective (orange) Hamiltonians before ($\eta = 5$) and after ($\eta = 0.5$) the exceptional entanglement transition. The blue empty circles are experimental data.

4. JOINT Q - R QUANTUM STATE TOMOGRAPHY

The joint Q - R output state after the NH dynamics is read out by mapping it to the Q_a - Q system. To accomplish this mapping, we must first transfer the state of Q to R_b . This is realized by tuning Q on resonance with R_b for a duration $t = \pi/(2g_b) = 12.5$ ns. After the $Q \rightarrow R_b$ state transfer, we reset Q to its idle frequency and bring Q_a resonance with R_b . Similarly, after an interaction duration t , Q_a carries the bus resonator's state. Up to this moment, we complete the state transfer from Q to Q_a .

The next step is to transfer the R -state to Q . Because the R -frequency is much higher than the Q 's, it is impossible to realize a quantum state transfer within the same short time period using the resonant coupling technique introduced above. As such, we consider the second-order sideband resonant coupling proposed in Section 2 instead. Limited by the experimental constraints, the maximum achievable coupling strength is about $\Omega_{max} = 2\pi \times 1.18$ MHz, which gives rise to the fastest state transfer time duration of approximately $\tau = 193$ ns. This period is comparable to the lifetime of the readout resonator so that the dissipation of R has a significant impact on the state mapping.

However, there is a one-to-one correspondence between the $Q_a Q$ output state after the state mapping and Q - R state just before the mapping for the no-jump case, as interpreted below. Without loss of the generality, the Q - R state right before the state mapping can be expressed as

$$|\psi_0\rangle = c_1|e, 0\rangle + c_2|g, 1\rangle, \quad (\text{S11})$$

with $|c_1|^2 + |c_2|^2 = 1$. After the state mapping, the Q_a - Q output state is

$$|\psi_1\rangle = (1/\sqrt{|c_1|^2 + k^2|c_2|^2})(c_1|e_a, g\rangle + kc_2|g_a, e\rangle), \quad (\text{S12})$$

where $k = e^{-\kappa t} e^{-\kappa\tau/4}$. For simplicity, we here do not include the phase accumulated during the mapping. This implies that the original Q - R output state $|\psi_0\rangle$ can be inferred from $|\psi_1\rangle$ by multiplying the coefficient of the component $|g_a, e\rangle$ by $1/k$ and then renormalizing the resulting state. In the experiment, the Q_a - Q output state is characterized by the two-qubit density matrix, which is reconstructed through joint quantum state tomography. The result associated with the no-jump trajectory is obtained by projecting the density matrix to the single-excitation subspace $\{|e_a, g\rangle, |g_a, e\rangle\}$, which can be expressed as

$$\rho_1 = \begin{pmatrix} \rho_{11} & \rho_{12} \\ \rho_{21} & \rho_{22} \end{pmatrix} \quad (\text{S13})$$

The elements of Q - R density matrix within $\{|e, 0\rangle, |g, 1\rangle\}$ right before the state mapping are related to those of ρ_1 by

$$\rho_1 = \frac{1}{\rho_{11} + \rho_{22}/k^2} \begin{pmatrix} \rho_{11} & \rho_{12}/k \\ \rho_{21}/k & \rho_{22}/k^2 \end{pmatrix} \quad (\text{S14})$$

5. QUBIT READOUT CORRECTIONS

The fidelity matrix for calibrating the measured probabilities is defined as

$$\hat{F} = \begin{pmatrix} F_g & e_{ge} \\ e_{eg} & F_e \end{pmatrix}, \quad (\text{S15})$$

where F_j ($j = g, e$) represents the probability for correctly reading out the state of the qubit when it is in $|k\rangle$, and e_{jk} ($j, k = g, e$) stands for the error that describes the leakage probability from the state $|k\rangle$ to state $|j\rangle$. To illustrate how the qubit readout error can be corrected, we denote the measured probability distribution as \hat{P}_M and the genuine probability distribution as \hat{P}_N . The relation among \hat{F} , \hat{P}_M , and \hat{P}_N is established by the following simple identity,

$$\hat{P}_M = \hat{F} \cdot \hat{P}_N. \quad (\text{S16})$$

The above relation (S16) implies that the genuine states of the system can be mathematically reconstructed by performing the matrix inversion of \hat{F} , i.e., $\hat{P}_N = \hat{F}^{-1} \cdot \hat{P}_M$. The data used in our calibrations are extracted from the measured I - Q (in phase and quadrature) values, as shown in Fig. S4. According to the measured data, in this work the fidelity matrices for Q and Q_a are

$$\hat{F}_Q = \begin{pmatrix} 0.981 & 0.099 \\ 0.019 & 0.901 \end{pmatrix}, \quad \hat{F}_{Q_a} = \begin{pmatrix} 0.977 & 0.098 \\ 0.023 & 0.902 \end{pmatrix}. \quad (\text{S17})$$

In the computational basis, the joint QST measurement on Q and Q_a can be therefore corrected by the following formula,

$$\hat{P}_N = (\hat{F}_Q \otimes \hat{F}_{Q_a})^{-1} \cdot \hat{P}_M. \quad (\text{S18})$$

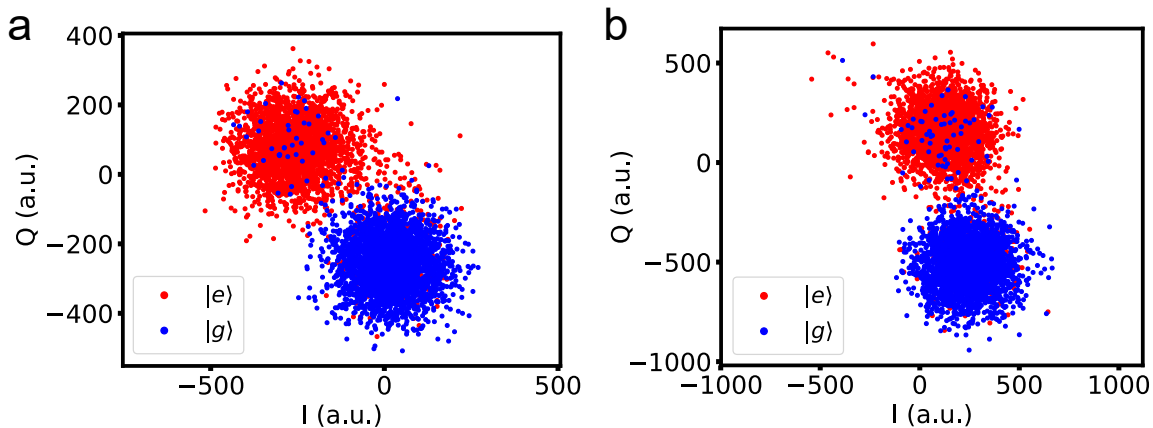


FIG. S4: **Qubit readouts for Q (a) and Q_a (b) with 3000 repetitions and 1.1- μ s readout duration.**

6. EXTRACTION OF EIGENENERGIES AND EIGENSTATES OF THE NON-HERMITIAN HAMILTONIAN

After collecting the data, we have applied the least-squares fitting to the measured density matrix ρ in order to extract the eigenenergies and eigenstates of the system. Theoretically, for a certain point in the parameter space, we can in principle write the eigenenergies and the corresponding eigenstates of the non-Hermitian system as

$$E_{\pm} = c_{\pm,1} + ic_{\pm,2}, \quad |\Phi_{\pm}\rangle = \alpha_{\pm}|g, 1\rangle + \beta_{\pm}|e, 0\rangle, \quad (\text{S19})$$

where $c_{\pm,1}$, $c_{\pm,2}$, α_{\pm} and β_{\pm} are the fitting parameters. If we assume the system's initial state to be

$$|e, 0\rangle = \frac{1}{\alpha_- \beta_+ - \alpha_+ \beta_-} (\alpha_- |\Phi_+\rangle - \alpha_+ |\Phi_-\rangle), \quad (\text{S20})$$

then at time t the system will evolve into the following state

$$|\psi(t)\rangle = \frac{1}{\alpha_- \beta_+ - \alpha_+ \beta_-} (\alpha_- e^{-iE_+ t} |\Phi_+\rangle + \alpha_+ e^{-iE_- t} |\Phi_-\rangle). \quad (\text{S21})$$

To minimize the fitting errors, we have defined an error function as a guidance, which has the form of

$$\text{erf} = \text{Tr}[\rho |\psi(t)\rangle \langle \psi(t)|] - 1. \quad (\text{S22})$$

Based on this error function, the next step is to seek the fitting parameters which can minimize Eq. (S22) at each moment. In this way, a reliable least-squares fitting to the entire evolution of the density matrix ρ is found with all the parameters: $c_{\pm,1}$, $c_{\pm,2}$, α_{\pm} , β_{\pm} .

The convergence condition is critical for ensuring the success of a fitting process. In Fig. S5, we show the convergence of residuals and all parameters as functions of the number of iterations. To facilitate comparison, we rescaled each parameter to an appropriate size, using $[f_i - f_N]/[\max(f) - \min(f)]$, where f represents the set of results after each iteration, f_i represents the result of the i -th iterations, and $i = 0, 1, 2, \dots, N$, with N being the maximum iteration number. We observe that all parameters converge together after a sufficient number of iterations. We provide two representative examples, one for $\eta = 5$ (above the EP, shown in Figs. S5a and b) and the other for $\eta = 0.5$ (below the EP, shown in Figs. S5c and d). We verified the validity of the remaining fitting procedures using the same approach.

We also calculate the fidelities of the eigenstates ($|\Phi'_{\pm}\rangle$) obtained in this manner with respect to the ideal ones $|\Phi_{\pm}\rangle$, which are defined as

$$\mathcal{F}_{\pm} = |\langle \Phi'_{\pm} | \Phi_{\pm} \rangle|^2. \quad (\text{S23})$$

The fidelities as functions of η are presented in Figs. S6a and b, respectively. The results demonstrate that the eigenstates, extracted from the measured two-qubit output density matrices by our density-matrix post-projecting method, well agree with the ideal ones, associated with the no-jump evolution trajectories. This agreement confirms the validity of approximations for deriving the effective NH Hamiltonian, as well as the soundness of the density-matrix post-projecting method.

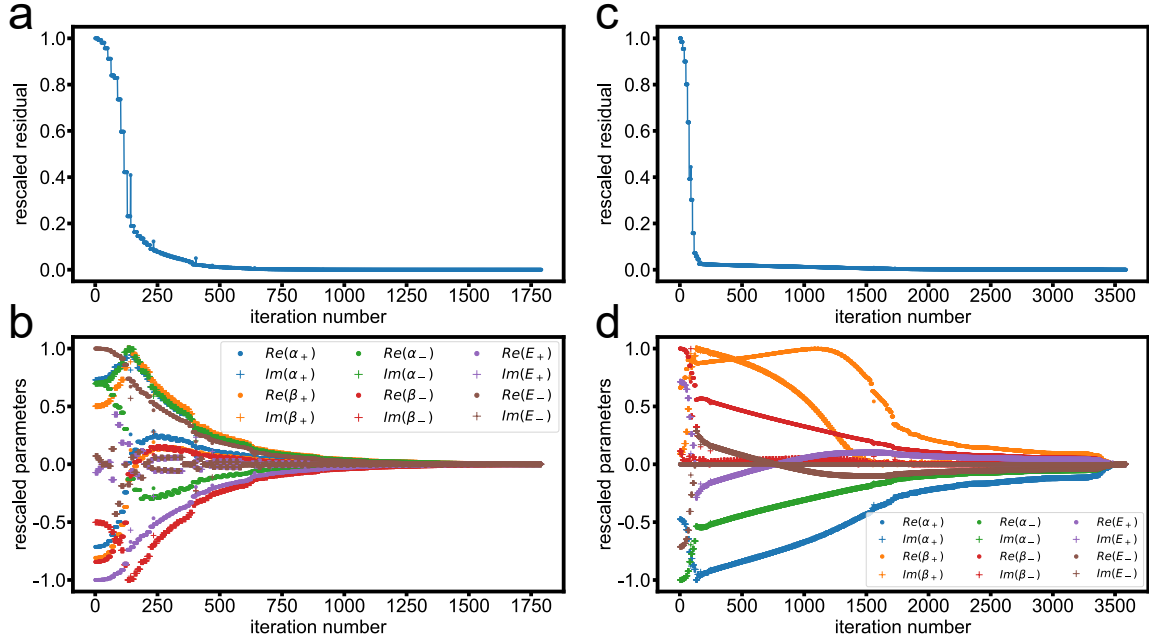


FIG. S5: Convergence of residuals and parameters. (a) (b) Above the EP, $\eta = 5$. (c) (d) Below the EP, $\eta = 0.5$.

7. PERFORMANCE OF THE NATURAL-DISSIPATION-ENHANCED QUANTUM SENSING

In our quantum sensing scheme, a slight deviation of the effective Q - R coupling from the EP $\Omega_0 = \kappa/4$, $\Delta\Omega = \Omega - \Omega_0$, is amplified by encoding it in the nonvanishing vacuum Rabi splitting E_G as

$$E_G = 2\Omega_0 \sqrt{2\Delta\Omega/\Omega_0 + (\Delta\Omega/\Omega_0)^2}. \quad (\text{S24})$$

When $\Delta\Omega \ll \Omega_0$, the terms $(\Delta\Omega/\Omega_0)^2$ can be neglected and thus $E_G \simeq 2\Omega_0 \sqrt{2\Delta\Omega/\Omega_0}$. The sensitivity enhancement is enabled by the square-root scaling of E_G with $\Delta\Omega$, which implies a divergent behavior of the changing rate of E_G at the EP. To further reveal this scaling, we plot the rescaled Rabi splitting $E_{G,R} = |E_G|/\Omega_0$ versus $\Delta\Omega_R = \Delta\Omega/\Omega_0$, and display the result in Fig. S7. The data are the same as those shown in Fig. 3d of the main text. Without including the unreasonable point (marked with 'X'), near the EP the result coincides with the square-root fitting (gray line): $E_{G,R} = 2\sqrt{2} (\text{Re} \sqrt{\Delta\Omega_R} + \text{Im} \sqrt{\Delta\Omega_R})$. We judge that the unusual deviation of the marked point from the fitting is due to the error for calibrating the value of Ω , interpreted as follows. At this point, the observed population of

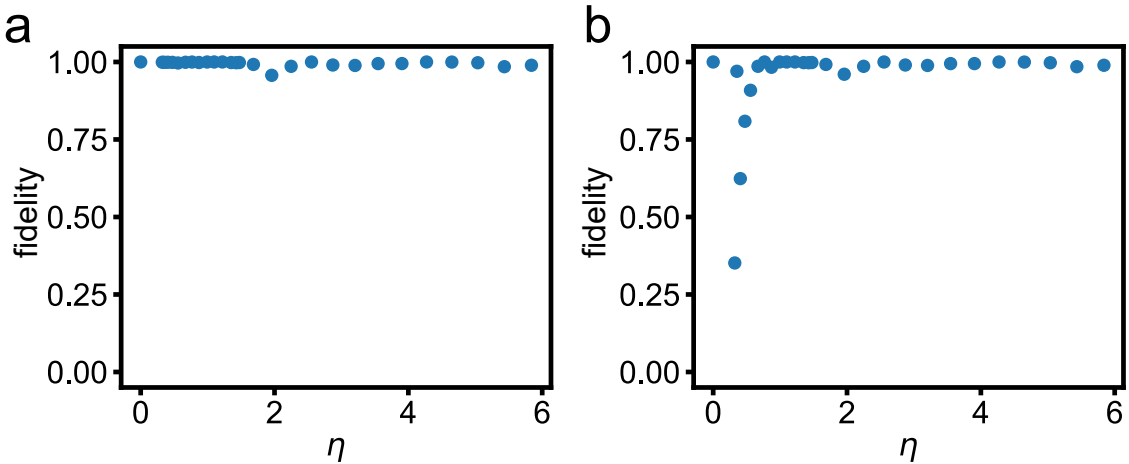


FIG. S6: Fidelities of fitted eigenstates. (a) \mathcal{F}_+ as a function of η . (b) \mathcal{F}_- as a function of η .

$|e, 0\rangle$ or $|g, 1\rangle$, associated with the no-jump trajectory, exhibits an oscillation pattern, manifested by the nonvanishing $\text{Re } E_G$. For $\Omega < \Omega_0$, the system cannot present such an evolution behavior, which implies the real value of Ω at this point is slightly larger than Ω_0 , but was pre-calibrated to be smaller than Ω_0 . With the increase of $\Delta\Omega$, the result progressively deviates from the square-root scaling owing to the non-negligible quadratic term in the radical sign. With this term being included, the ideal result is given by

$$E_{G,R} = |2\sqrt{2\Delta\Omega_R + (\Delta\Omega_R)^2}|. \quad (\text{S25})$$

The coincidence between the experiment results with this formula (blue dashed line) verifies a good control of the system, as well as the stability of the natural dissipation as a useful resource for quantum sensing.

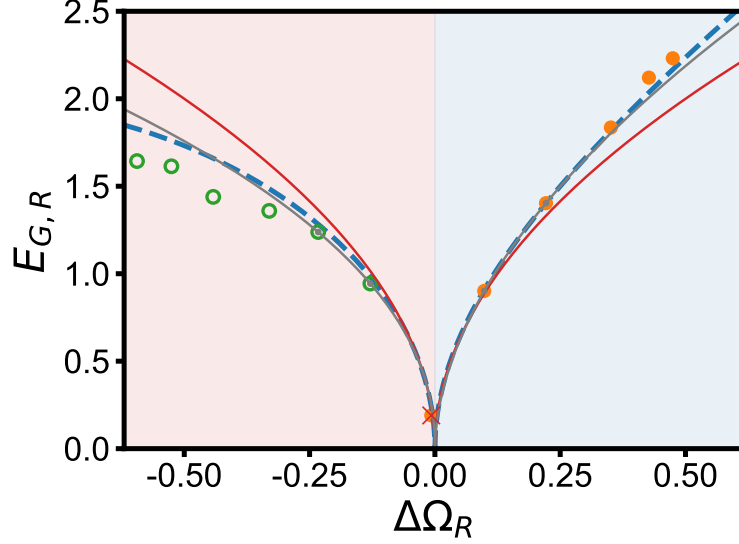


FIG. S7: **The power-law relationship between $E_{G,R}$ and $\Delta\Omega_R$.** The blue dashed line represents the result given by Eq. (S25), the red line shows the ideal square-root behavior and the gray line is fitted with the experimental data.

In the vicinity of the EP, the rescaled Rabi splitting exhibits a square-root dependence on $\Delta\Omega_R$, as given by $E_{G,R} = 2\sqrt{2}\sqrt{|\Delta\Omega_R|}$. To confirm this behavior with the experimental data shown in Fig. S7, we fit the data with a power-law function of the form $E_{G,R} = A(|\Delta\Omega_R|)^B$, where the exponent B characterizes the response strength. The gray line in Fig. S7 stands for the fit to the experimental data, which yields the parameter values of $A = 3.192$ and $B = 0.545$ for $\Delta\Omega_R > 0$, and $A = 2.415$ and $B = 0.459$ for $\Delta\Omega_R < 0$. The well agreement between the fitted functions and the measured results near the EP (except the unreasonable point) implies that the natural dissipation indeed serves as a useful resource for amplifying the signal produced by a weak field.

8. EXCEPTIONAL ENTANGLEMENT TRANSITION IN A TWO-QUBIT SYSTEM

The exceptional entanglement transition is not restricted to the light-matter system, but is a universal behavior for a variety of NH interacting quantum systems. As a paradigmatic example, we here consider the system composed of two decaying qubits interacting with each other by swapping coupling [51-53]. When the two qubits have the same frequency, the no-jump evolution trajectory is governed by the NH Hamiltonian (setting $\hbar = 1$)

$$\mathcal{H}_{NH} = \Omega(\sigma_1^+ \sigma_2^- + \sigma_1^- \sigma_2^+) - \frac{i}{2}(\kappa_1 |e_1\rangle \langle e_1| + \kappa_2 |e_2\rangle \langle e_2|), \quad (\text{S26})$$

where $\sigma_j^+ = |e_j\rangle \langle g_j|$ and $\sigma_j^- = |g_j\rangle \langle e_j|$ with $|e_j\rangle$ ($|g_j\rangle$) denoting the upper (lower) level of the j th qubit, κ_j is the dissipation rate of $|e_j\rangle$, and Ω is coupling strength. This swapping coupling does not change the total excitation number of the system. When the system is initially in a one-excitation state, its dynamics will be restricted within the subspace $\{|e_1, g_2\rangle, |g_1, e_2\rangle\}$. In such a subspace, the eigenstates of the NH Hamiltonian are given by

$$|\Phi_{\pm}\rangle = \mathcal{N}_{\pm}(\Omega |e_1, g_2\rangle + \Gamma_{\pm} |g_1, e_2\rangle), \quad (\text{S27})$$

where $\Gamma_{\pm} = -i\kappa/4 \pm E_g/2$ with $\kappa = \kappa_2 - \kappa_1$. The energy gap between these two eigenstates is $E_G = 2\sqrt{\Omega^2 - \kappa^2}/16$.

When the two qubits have distinct decaying rates, these eigenstates and eigenenergies have the same forms as those of the qubit-resonator system. Consequently, the energy gap undergoes a real-to-imaginary transition at the EP $\eta = 4\Omega/|\kappa| = 1$, which is accompanied by an entanglement transition of the eigenstates. The two-qubit concurrences [40] for the two eigenstates $|\Phi_{\pm}\rangle$ are

$$\mathcal{E}_{\pm} = \frac{2\Omega|\Gamma_{\pm}|}{|\Gamma_{\pm}|^2 + \Omega^2}. \quad (\text{S28})$$

When $\eta \rightarrow 0$, the two eigenstates respectively reduce to $|e_1, g_2\rangle$ and $|g_1, e_2\rangle$, each of which has no entanglement. The concurrence is increased linearly with η until reaching the EP, where the energy gap vanishes and both eigenstates converge to the same maximally entangled state

$$|\Phi_{\pm}\rangle = (|e_1, g_2\rangle - i|g_1, e_2\rangle)/\sqrt{2}. \quad (\text{S29})$$

After crossing the EP, $|\Phi_{\pm}\rangle$ move in opposite directions, but with the concurrences \mathcal{E}_{\pm} remaining to be 1, independent of η .